

Accepted Article Preview: Published ahead of advance online publication



Achromatic super-oscillatory lenses with sub-wavelength focusing

Guang Hui Yuan, Edward TF Rogers and Nikolay I Zheludev

Cite this article as: Guang Hui Yuan, Edward TF Rogers and Nikolay I Zheludev. Achromatic super-oscillatory lenses with sub-wavelength focusing. *Light: Science & Applications* accepted article preview 7 March 2017; doi: 10.1038/lisa.2017.36

This is a PDF file of an unedited peer-reviewed manuscript that has been accepted for publication. NPG are providing this early version of the manuscript as a service to our customers. The manuscript will undergo copyediting, typesetting and a proof review before it is published in its final form. Please note that during the production process errors may be discovered which could affect the content, and all legal disclaimers apply.

Received 20 December 2016; revised 2 March 2017; accepted 5 March 2017;
Accepted article preview online 7 March 2017

Achromatic super-oscillatory lenses with sub-wavelength focusing

Running title: Super-oscillatory achromatic lenses

Guang Hui Yuan^{1#}, Edward T. F. Rogers^{2,3}, and Nikolay I. Zheludev^{1,2*}

¹*Centre for Disruptive Photonic Technologies, The Photonic Institute, SPMS, Nanyang Technological University, Singapore 637371, Singapore*

²*Optoelectronics Research Centre and Centre for Photonic Metamaterials, University of Southampton, Highfield, Southampton, SO17 1BJ, UK*

³*Institute for Life Sciences, University of Southampton, Highfield, Southampton, SO17 1BJ, UK*

Email addresses:

Guang Hui Yuan: ghyuan@ntu.edu.sg

Edward T. F. Rogers: etr@orc.soton.ac.uk

Nikolay I. Zheludev: nzheludev@ntu.edu.sg

**Corresponding author 1:*

Nikolay I. Zheludev:

*Centre for Disruptive Photonic Technologies,
School of Physical & Mathematical Sciences,
SPMS-PAP-01-28,
Nanyang Technological University,
Nanyang Link 21, Singapore 637371
Contact: +65-6513-8493*

#Corresponding author 2:

Guang Hui Yuan:

*Centre for Disruptive Photonic Technologies,
School of Physical & Mathematical Sciences,
SPMS-PAP-01-28,
Nanyang Technological University,
Nanyang Link 21, Singapore 637371
Contact: +65-6592-3568*

Abstract:

Lenses are crucial to light-enabled technologies. Conventional lenses have been perfected to achieve near-diffraction-limited resolution and minimal chromatic aberrations. However, such lenses are bulky and cannot focus light into a hotspot smaller than a half-wavelength of light. Pupil filters, initially suggested by Toraldo di Francia, can overcome the resolution constraints of conventional lenses but are not intrinsically chromatically corrected. Here, we report single-element planar lenses that not only deliver sub-wavelength focusing, thus beating the diffraction limit of conventional refractive lenses, but also focus light of different colors into the same hotspot. Using the principle of super-oscillations, we designed and fabricated a range of binary dielectric and metallic lenses for visible and infrared parts of the spectrum that are manufactured on silicon wafers, silica substrates and optical fiber tips. Such low-cost, compact lenses could be useful in mobile devices, data storage, surveillance, robotics, space applications, imaging, manufacturing with light, and spatially resolved nonlinear microscopies.

Keywords: achromatic; super-oscillation; super-resolution.

INTRODUCTION

Chromatic aberration and the resolution limit are two major challenges for high-performance optical imaging. Chromatic aberration (chromatism) is a failure of the lens to focus all colors on the same point. In refractive focusing devices, it results from dispersion of the lens material. In diffractive focusing devices, chromatic aberration results from the accumulated wavelength-dependent phase delay of the electromagnetic waves that form the focus. To reduce chromatic aberrations, complex optical elements such as achromatic doublet, triplet and diffractive-refractive hybrid lenses have been built^{1,2} with components of opposing dispersion properties³. However, such lenses are inevitably bulky, which complicates integration. Several approaches have been proposed to miniaturize beam-shaping and focusing devices including planar Fresnel zone plates and, more recently, metasurface-based plasmonic and dielectric lenses and axicons⁴⁻¹². However, chromatism remains a key challenge, which has been tackled using dielectric metasurfaces^{13,14} and wavelength-independent geometric phases¹⁵ and by exploiting the inherent dispersion in diffractive optics¹⁶.

The other key parameter of an imaging system is its spatial resolution: the ability to resolve details of the object that is being imaged. It is commonly believed that the resolution of an optical system that images objects from the far-field to the far-field of the lens is limited to half the optical wavelength (the Abbe-Rayleigh diffraction limit) due to the loss of fine detail for the electromagnetic field distribution near the object. Indeed, the Abbe-Rayleigh diffraction limit was viewed as the main obstacle to the development of sub-wavelength-resolution label-free microscopy. Powerful alternative approaches for super-resolution fluorescent bio-imaging have been developed. These include stimulated emission depletion microscopy (STED), which uses two beams, one to excite and the other to deplete luminescence¹⁷; photo-activated localization microscopy (PALM); and stochastic optical

reconstruction microscopy (STORM), which is based on localizing single luminescent molecules in the imaged object^{18,19}. A common feature of these techniques is the use of fluorescent labels embedded in the object that make them suitable for only a narrow group of applications, predominantly in biology.

Many important technological challenges, from next-generation lithography to data storage and fabrication with light, could be solved if a focusing system existed that could beat the Abbe–Rayleigh diffraction limit and create hotspots much smaller than the wavelength of light. The existence of the resolution limit has been challenged by the promising idea of a far-field to far-field superlens fabricated from a material with a negative index of refraction²⁰. Such a superlens could “translate” both the propagating waves and evanescent waves in the immediate proximity of the object into the remote image. Although simpler devices imaging from the near-field to the near-field²¹ and from the near-field to the far-field^{22,23} have been successfully demonstrated, a negative index superlens that images from the far-field to the far-field has not yet been developed for the optical part of the spectrum and would likely inherit chromatic aberration from the dispersion of the negative index medium.

As originally proposed by Toraldo di Francia, focusing beyond the Abbe–Rayleigh diffraction limit can be achieved by a pupil filtering technique²⁴⁻²⁷. From the perspective of modern wave theory, this approach exploits the phenomenon of optical super-oscillations²⁸⁻³⁸, in which a complex band-limited signal can locally oscillate much faster than its highest Fourier components³⁹⁻⁴¹, and thus the accurately tailored interference of waves can form foci smaller than the size allowed by the Abbe–Rayleigh diffraction limit. Mathematically, according to M.V. Berry, this can be explained by the fact that “In the Wigner representations of the local Fourier transform in the ‘phase space’ Wigner function can have both positive and negative values, which causes subtle cancellations in the Fourier integration over all of the function”⁴². In super-oscillatory focusing and imaging devices, fine details of the

electromagnetic field near the object are conveyed to the image by the propagating waves themselves, an effect the conventional Abbe–Rayleigh theory deemed impossible since the spatial spectrum of free-space waves is limited by the free-space wavevector.

This work is devoted to the development of achromatic super-oscillatory sub-wavelength focusing devices. We explore planar masks that convert light waves into super-oscillatory foci by the use of tailored interference of waves diffracted from different areas of the mask (termed a ‘super-oscillatory lens’, SOL). To create super-oscillatory foci, both amplitude and phase masks can be used. Although the outcome of interference is wavelength-dependent, an SOL can be designed to focus different wavelengths into the same spot (see Fig.1). This is possible because the SOL can create foci of extremely long depths, extending tens of wavelengths^{33,43,44}, and so foci of different wavelengths can partially overlap, creating a zone of distances from the SOL where a range of colors can be focused simultaneously. An alternative approach is to use a super-oscillatory mask that generates several discrete foci at different distances from it. For different wavelengths, some of these foci can overlap, and so the SOL will focus two or more wavelengths simultaneously in one spot.

Below, we will describe a range of SOLs, demonstrating the wide variety of lenses that can be designed and the flexibility possible in designing lenses for particular applications. We have made both amplitude- and phase-modulated achromatic SOLs for visible and infrared radiation and an apochromatic red/green/blue SOL for the visible part of the spectrum. Here and below, we adopt the well-established terminology¹⁻³ that a lens is called achromatic if it brings two wavelengths into focus in the same plane and apochromatic if it focuses three wavelengths simultaneously.

MATERIALS AND METHODS

Achromatic SOL design procedure.

For the design of achromatic SOLs, we used the **multi-objective** particle swarm optimization (PSO) algorithm⁴⁵, which optimizes a problem regarding a given merit function using a population of ‘particles’ in the N -dimensional search space. For a ring mask, the radial direction is divided into N equally spaced zones. Each zone has either a unit (‘1’) or zero (‘0’) value, which corresponds to transparent and opaque for the amplitude mask, and two phase levels for the phase mask. The PSO algorithm searches for the best arrangement of these binary values. **In contrast to our previous works^{30,33,36}, here**, the target function to describe the electric field intensity profiles near the focus for individual wavelength λ_p is defined as

$$I_p^{tar}(\lambda_p, r, z) = \left[\frac{2J_1(a_p r)}{a_p r} \right]^2 \exp \left[-\frac{(z-z_f)^2}{b_p^2} \right] \quad (1)$$

where p is the numbering of wavelengths, $J_1(x)$ is the first-order Bessel function of the first kind, z_f is the desired achromatic working distance, $a_p = \frac{3.233}{FWHM_p}$, $b_p = \frac{DOF_p}{2\sqrt{\ln 2}}$, $FWHM_p$ is the full-width half-maximum of the transverse hotspot size, and DOF_p is the depth of focus at λ_p . The merit function to achieve the achromatic SOL design is given as

$$F(r, z) = \sum_{\lambda_p} |I_p^{act}(\lambda_p, r, z) - I_p^{tar}(\lambda_p, r, z)|^2 \quad (2)$$

where $I_p^{act}(\lambda_p, r, z)$ is the normalized actual intensity distribution at λ_p and is calculated by the angular spectrum method for a given mask design. The optimal SOL mask is achieved after sufficient iterations to allow $F(r, z)$ **to reach its minimum value.**

SOL sample preparation and fabrication.

All SOLs were fabricated by focused ion beam milling (Helios 650, Hillsboro, OR, USA).

For the binary amplitude mask, a 100 nm-thick gold film was deposited on a silica glass

substrate using a thermal evaporator (Oerlikon Univex 250, Cologne, Germany) with a deposition rate of 0.2 Å/s. Prior to deposition of the gold, a 5 nm-thick chromium adhesion layer was deposited on the substrate. For the fiberized SOL, the fabrication process remains essentially the same, while the photonic crystal fibers (LMA35, NKT photonics, Birkerød, Denmark) are cleaved with a large-diameter fiber cleaver (VYTRAN LDC-400, Thorlabs Inc., Newton, NJ, USA). A careful alignment between the centers of the SOL and fiber core must be achieved for correct performance of the SOL. For the dielectric SOL, FIB writing is conducted directly onto the silicon wafer (University Wafer Inc., DSP, 100, p-type).

RESULTS AND DISCUSSION

Near-IR achromatic fiberized amplitude mask SOL

A sub-wavelength focusing, near-IR lens on a fiber tip would be valuable in many applications, most notably imaging through silicon wafers and substrates inside silicon chips, diagnostics of optoelectronic devices, high-resolution two-photon polymerization nanofabrication, non-destructive imaging of in-vitro biomedical samples, micro-spectrometry of molecular vibrational modes, and an interconnect element of silicon photonic devices. We chose the tip of a single-mode large-mode-area photonic crystal fiber (PCF, NKT photonics) as the platform for our achromatic near-infrared SOL. The advantage of such fibers is that they provide a stable high-quality mode, even at high output power, and single-mode operation with almost constant mode diameter for broadband wavelengths—which is useful, though not essential—when designing achromatic devices.

The SOL is a concentric ring nanostructure located in the middle of the PCF cross-section (see SEM micrograph in Fig. 2a). It is optimized to be achromatic at two telecommunication wavelengths $\lambda_{\text{IR1}}=1.3 \mu\text{m}$ and $\lambda_{\text{IR2}}=1.55 \mu\text{m}$. The design and optimization procedures, and the fabrication process, are described in the Methods section below (see Supplementary

Information-Section 1 for the design parameters of all SOLs used in this paper). The theoretical focusing performance for the chosen wavelengths—calculated by the angular spectrum method³⁰—is shown in Figs. 2b1 and 2b3. Calculations reveal that at $\lambda_{\text{IR1}}=1.3 \mu\text{m}$, the SOL produces an “optical needle”, a long focal spot extending from an axial distance of $6.1 \mu\text{m}$ to $11.9 \mu\text{m}$, while at $\lambda_{\text{IR2}}=1.55 \mu\text{m}$, the “optical needle” extends from $3.1 \mu\text{m}$ to $9.7 \mu\text{m}$ from the lens. Here, achromatic performance can be expected from $6.1 \mu\text{m}$ to $9.7 \mu\text{m}$, centered at a working distance of approximately $8 \mu\text{m}$.

To experimentally characterize the lens, we first measured the mode field diameter of the fiber and found it to be $26 \mu\text{m}$ for both wavelengths of interest, $\lambda_{\text{IR1}}=1.3 \mu\text{m}$ and $\lambda_{\text{IR2}}=1.55 \mu\text{m}$, as shown in the inset of Fig. 2a. A conventional glass lens with a diameter of $26 \mu\text{m}$ and focal distance of $8 \mu\text{m}$ would have a numerical aperture of $\text{NA}=0.85$. Since the superoscillatory field structure of the lens is formed by free-space waves, it can be imaged with a lens of similar or higher numerical aperture. The lens was characterized with a tunable supercontinuum laser source coupled into the fiber and a high-resolution InGaAs camera equipped with an objective of $\text{NA}=0.95$ (see Supplementary Information-Section 2 for the experimental details). The intensity pattern after the SOL was recorded slice by slice with an axial step of 200 nm (see Figs. 2b2 and 2b4). The optical needles are located between $5.4 \mu\text{m}$ and $10.8 \mu\text{m}$ for λ_{IR1} and between $3.4 \mu\text{m}$ and $10.4 \mu\text{m}$ for λ_{IR2} , showing reasonable agreement with simulations. The fractions of energy focused into the sub-wavelength hotspots at the target plane at $8 \mu\text{m}$ were found to be 2.9% and 2.1% for λ_{IR1} and λ_{IR2} , respectively.

The cross-sections of the hotspots at $8 \mu\text{m}$ from the lens are presented in Fig. 2c. At $\lambda_{\text{IR1}}=1.3 \mu\text{m}$, the full-width at half-maximum (FWHM) in the simulation was $0.47 \times \lambda_{\text{IR1}}$ compared to the experimental observation of $(0.51 \pm 0.02) \times \lambda_{\text{IR1}}$. At $\lambda_{\text{IR2}}=1.55 \mu\text{m}$, the FWHM of the predicted hotspot was $0.44 \times \lambda_{\text{IR2}}$ compared to the experimental observation of

$(0.48 \pm 0.02) \times \lambda_{\text{IR}2}$. A normal glass lens of equivalent size would not be able to deliver such sharp focus: its focal spot would be at least the Abbe–Rayleigh diffraction limit of 0.59λ .

We used two approaches to prove that the generated fields are actually super-oscillatory: one confirms that the spatial spectra of the hotspots are beyond the available band-limited spectrum of the overall field, and the other shows that the local wavevectors are locally much larger than the highest wavevector of the light (see Supplementary Information-Section 3 for the details).

Near-IR achromatic silicon phase-mask SOL

Similar achromatic focusing can be achieved with a dielectric phase mask. Low-loss dielectric phase masks can simultaneously improve the throughput efficiency of the lens and dramatically enhance optical breakdown thresholds of the device for both CW and pulsed illumination. We chose to work with silicon because it is compatible with the fabrication process of well-established technologies. Here, we used focused ion beam milling, although high-resolution optical and electron beam lithography would give similar or even better results. By milling different depths into a silicon wafer, we created a lossless dielectric achromatic SOL for the same telecommunication wavelengths of $\lambda_{\text{IR}1}=1.3 \mu\text{m}$ and $\lambda_{\text{IR}2}=1.55\mu\text{m}$. The refractive indices at $\lambda_{\text{IR}1}$ and $\lambda_{\text{IR}2}$ were measured to be 3.509 and 3.481, respectively (see Supplementary Information-Section 4 for the n–k curves), and the material's dispersion was considered during the mask optimization. At a milling depth of 312 nm, a step in the silicon layer creates a phase retardation of 1.2π at $\lambda_{\text{IR}1}=1.3 \mu\text{m}$ and π at $\lambda_{\text{IR}2}=1.55 \mu\text{m}$. The SEM micrograph of an SOL is shown in Fig. 3a.

The computed and experimentally measured focusing performance of the lens is presented in Fig. 3b. The super-oscillatory hotspots can be observed near an axial distance of $20 \mu\text{m}$, where at $\lambda_{\text{IR}1}$, the theoretical depth of focus is $6.7 \mu\text{m}$, compared with the experimental value

of 5.2 μm . At $\lambda_{\text{IR}2}$, we obtained 5.4 μm and 5.8 μm for the computed and experimentally observed depths of focus, respectively. At 20 μm from the lens, the hotspot size at $\lambda_{\text{IR}1}=1.3$ μm was $0.427\times\lambda_{\text{IR}1}$ (simulation, blue curve) and $(0.42\pm 0.04)\times\lambda_{\text{IR}1}$ (experiment); see Fig. 3c. Similarly, for $\lambda_{\text{IR}2}$, the FWHM of the hotspot was $0.435\times\lambda_{\text{IR}2}$ (simulation) and $(0.44\pm 0.02)\times\lambda_{\text{IR}2}$ (experiment); see Fig. 3d. The fractions of energy focused into the sub-wavelength hotspots at the target plane at 20 μm were found to be 1.26% and 2.1% for $\lambda_{\text{IR}1}$ and $\lambda_{\text{IR}2}$, respectively. **For comparison, the diffraction limit is $0.56\times\lambda$.**

Visible achromatic amplitude mask SOL

Interference-based super-oscillatory focusing is scalable to any wavelength. An SOL working at a shorter wavelength places greater demand on the finesse and accuracy of fabrication, but we show here that it is still possible to manufacture visible-wavelength achromatic SOLs by focused ion beam milling. As examples, we have chosen two wavelengths of $\lambda_1=690$ nm and $\lambda_2=870$ nm, one in the visible band and the other in the infrared band. These or similar wavelengths are often used in nonlinear optical imaging techniques and spectroscopic pump-probe experiments, particularly with the widespread Ti:sapphire laser sources.

The mask is shown in Fig. 4a. Simulated field patterns in the central cross-sections along (xz plane) and perpendicular to the incident polarization (yz plane) are shown in Fig. 4b. The incident beam is an x -polarized plane wave. Achromatic performance is centered at $z_f=18$ μm , where an elongated hotspot at $\lambda_1=690$ nm (15 μm to 20.1 μm) overlaps with a hotspot at $\lambda_2=870$ nm (16 μm to 19.9 μm) for λ_2 . The FWHMs of the hotspots are 280 nm ($0.405\times\lambda_1$) and 367 nm ($0.422\times\lambda_2$) for λ_1 and λ_2 , respectively, and are sub-diffraction-limited. For a conventional lens of this size, the diffraction-limited hotspot ($0.548\times\lambda$) will be 378 nm at $\lambda_1=690$ nm and 477 nm at $\lambda_2=870$ nm.

The experimentally measured field structures are presented in Fig. 4b2 and Fig. 4b4. Hotspots with comparable depths of focus are generated at $z_f = 18 \mu\text{m}$, which is in agreement with the theoretical predictions. At $\lambda_1 = 690 \text{ nm}$, the observed dimensions of the hotspots were $0.42 \times \lambda_1$ for the direction along the incident polarization and $0.46 \times \lambda_1$ for the perpendicular direction. For $\lambda_2 = 870 \text{ nm}$, the spot sizes were $0.43 \times \lambda_2$ and $0.44 \times \lambda_2$ in the two directions, respectively; see Fig. 4c2 and Fig. 4c4. The fractions of energy focused into the sub-wavelength hotspots at the target plane at $18 \mu\text{m}$ were found to be 0.47% and 1% for λ_1 and λ_2 , respectively.

Here, we note that the conventional binary Fresnel zone plate is highly dispersive, and its focal distance will depend on the wavelength, progressively shifting away from the lens for longer wavelengths. Thus, the Fresnel zone plate cannot offer an achromatic solution (see Supplementary Information-Section 5).

RGB ‘white’-light apochromatic amplitude mask SOL

We found that designing a single-element lens that focuses light across the entire visible range into a single hotspot is difficult (see the previous SOL performance for the intermediate wavelengths between λ_1 and λ_2 in Supplementary Information-Section 6). However, we have been able to design an SOL that simultaneously focuses the three primary colors of the additive model that together can produce perceived white light. We have developed an apochromatic SOL for red ($\lambda_R = 633 \text{ nm}$), green ($\lambda_G = 532 \text{ nm}$) and blue ($\lambda_B = 405 \text{ nm}$) light, as illustrated in Fig. 5a. It is well known from computer display and digital imaging technology that any perceived color can be generated by combining these three colors.

Figure 5b shows an SEM micrograph of the mask. We targeted a working distance of $10 \mu\text{m}$ and an FWHM of $0.4 \times \lambda$, which is 28% less than the diffraction limit of $0.56 \times \lambda$. The simulated intensity profiles in the longitudinal cross-section are given in Fig. 5c. The corresponding experimental data are shown in Fig. 5d. The field structures in the focal plane

for R, G, and B wavelengths are displayed in Figs. 5e1–5e3. The simulated hotspot sizes were $0.438 \times \lambda_R$ at $\lambda_R=633$ nm, $0.422 \times \lambda_G$ at $\lambda_G=532$ nm and $0.523 \times \lambda_B$ at $\lambda_B=405$ nm. Experimentally we obtained hotspots of $(0.457 \pm 0.01) \times \lambda_R$, $(0.445 \pm 0.04) \times \lambda_G$ and $(0.54 \pm 0.03) \times \lambda_B$, respectively. The fractions of energy focused into the sub-wavelength hotspots at the target plane were found to be 1.35%, 1.18% and 1.54% for λ_R , λ_G , and λ_B , respectively.

As expected, we could acquire a ‘white’ super-oscillatory hotspot by focusing supercontinuum fiber laser radiation that was spectrally conditioned at the selected RGB wavelengths by a programmable acousto-optic tunable filter; see Fig. 5e4. **Notably, superachromatic SOLs that work for more than three wavelengths are also possible and can be designed in a similar way. We give an example of an SOL working for four wavelengths in Supplementary Information-Section 7.**

CONCLUSIONS

We experimentally demonstrated that chromatic aberration and the optical diffraction limit can be simultaneously overcome using an SOL consisting of a single planar optical element. The single-element SOL creates sub-diffraction hotspots by delicate constructive interference of propagating optical waves with different wavevectors and therefore allows foci at different wavelengths to spatially overlap in an achromatic fashion.

Sub-wavelength focusing of SOLs comes at a price. Only a small fraction of light incident on the lens is actually focused in the central hotspot, while the remaining fraction is mainly distributed in broad “halo” rings around the hotspot. For some applications, the effect of a halo can be eliminated. For instance, in imaging, light scattered by a halo can be suppressed using a confocal technique³⁰, while in heat-assisted magnetic recording applications, it can be illuminated by using additional thin apertures⁴⁶. In some nonlinear optical applications such

as coherent anti-Stokes Raman spectroscopy (CARS)⁴⁷, suppression of the halo comes naturally through nonlinear interactions at different frequencies. Although we did not consider the energy concentration problem during our SOL design process, it would be possible to incorporate it into the same framework⁴⁸. Increasing the dimension number N would give more degrees of freedom for maximization of energy concentration, especially for multiple wavelengths. For phase-type SOLs, increasing the number of phase levels would be helpful to reduce the sidebands and increase the focusing efficiency of super-oscillatory hotspots.

In the focusing devices described here, 1% to 3% of incident energy is focused in the central hotspot, while the intensity level could be a factor of 3 higher than the intensity level of the incident wave onto the lens, as, for instance, in the fiberized lens described above. The low level of throughput efficiency may be prohibitive for some demanding applications but may be tolerable for others. For instance, a low-loss dielectric SOL that is 40 μm in diameter will be able to sustain incident CW laser radiation of a few watts, corresponding to focal intensities of a few hundred kW/cm^2 . When used with pulsed lasers, the lens will be able to sustain a few hundred mJ/cm^2 of incident fluence with femtosecond and picosecond pulses and up to a few J/cm^2 with nanosecond pulses^{49,50}. It will deliver a similar level of energy density in the hotspot. Such levels of optical excitations will be overwhelmingly sufficient for raster imaging, lithography and nanofabrication with light.

We fabricated metallic and dielectric binary amplitude and phase masks that are wavelength scalable and can work for different spectral bands. In the infrared band, we implemented achromatic SOLs at the tip of large-mode-area single-mode photonic crystal fibers and on silicon wafers. For the visible band, we developed an achromatic SOL for two well-separated wavelengths and an apochromatic SOL for RGB wavelengths suitable for creating a sub-diffraction ‘white’ hotspot.

We anticipate that achromatic sub-diffraction photonic focusing devices could serve as super-resolved focusing and imaging tools for a broad range applications in nonlinear optics, photography, retinal diagnostics⁵¹, low-cost fiberized microscopy, non-invasive and label-free biological imaging, pump-probe experiments for ultrafast dynamics, excitation and collection of photoluminescence, coherent anti-Stokes Raman scattering for super-resolution bio-imaging, nonlinear imaging and nanofabrication using two/three-photon generation.

ACKNOWLEDGMENTS

This work was supported by the Agency for Science, Technology and Research (A*STAR) of Singapore (Grants 122-360-0009), the Singapore Ministry of Education (Grant MOE2011-T3-1-005), the Engineering and Physical Sciences Research Council UK (Grants EP/F040644/1 and EP/M009122/1) and the University of Southampton Enterprise Fund. The authors thank X. H. Li and L. B. Wang for assistance with fiber cleaving, G. Adamo and H. Krishnamoorthy for ellipsometry measurements of silicon wafers, and P. Smith for fruitful discussions. The data from this paper can be obtained from the University of Southampton ePrints research repository: <http://dx.doi.org/10.5258/SOTON/394664>.

REFERENCES

- 1 Wang YX, Yun WB, Jacobsen C. Achromatic Fresnel optics for wideband extreme-ultraviolet and X-ray imaging. *Nature* 2003; **424**: 50-53.
- 2 Greisukh GI, Ezhov EG, Stepanov SA. Diffractive–refractive hybrid corrector for achro- and apochromatic corrections of optical systems. *Appl Opt* 2006; **45**: 6137-6141.
- 3 Mikš A, Novák J. Method for primary design of superachromats. *Appl Opt* 2013; **52**: 6868-6876.
- 4 Lin DM, Fan PY, Hasman E, Brongersma ML. Dielectric gradient metasurface optical elements. *Science* 2014; **345**: 298-302.
- 5 Verslegers L, Catrysse PB, Yu ZF, White JS, Barnard ES *et al*. Planar lenses based on nanoscale slit arrays in a metallic film. *Nano Lett* 2008; **9**: 235-238.

- 6 Ishii S, Shalaev VM, Kildishev AV. Holey-metal lenses: sieving single modes with proper phases. *Nano Lett* 2012; **13**: 159-163.
- 7 Chen XZ, Huang LL, Mühlenbernd H, Li GX, Bai BF *et al.* Dual-polarity plasmonic metalens for visible light. *Nat Commun* 2012; **3**: 1198.
- 8 Aieta F, Genevet P, Kats MA, Yu NF, Blanchard R *et al.* Aberration-free ultrathin flat lenses and axicons at telecom wavelengths based on plasmonic metasurfaces. *Nano Lett* 2012; **12**: 4932-4936.
- 9 Ni XJ, Ishii S, Kildishev AV, Shalaev VM. Ultra-thin, planar, Babinet-inverted plasmonic metalenses. *Light Sci Appl* 2013; **2**: e72.
- 10 Pors A, Nielsen MG, Eriksen RL, Bozhevolnyi SI. Broadband focusing flat mirrors based on plasmonic gradient metasurfaces. *Nano Lett* 2013; **13**: 829-834.
- 11 Fattal D, Li JJ, Peng Z, Fiorentino M, Beausoleil RG. Flat dielectric grating reflectors with focusing abilities. *Nat Photonics* 2010; **4**: 466-470.
- 12 Arbabi A, Horie Y, Ball AJ, Bagheri M, Faraon A. Subwavelength-thick lenses with high numerical apertures and large efficiency based on high-contrast transmitarrays. *Nat Commun* 2015; **6**: 7069.
- 13 Aieta F, Kats MA, Genevet P, Capasso F. Multiwavelength achromatic metasurfaces by dispersive phase compensation. *Science* 2015; **347**: 1342-1345.
- 14 Arbabi E, Arbabi A, Kamali SM, Horie Y, Faraon A. Multiwavelength polarization-insensitive lenses based on dielectric metasurfaces with meta-molecules. *Optica* 2016; **3**: 628-633.
- 15 Zhao ZY, Pu MB, Gao H, Jin JJ, Li X *et al.* Multispectral optical metasurfaces enabled by achromatic phase transition. *Sci Rep* 2015; **5**: 15781.
- 16 Wang P, Mohammad N, Menon R. Chromatic-aberration-corrected diffractive lenses for ultra-broadband focusing. *Sci Rep* 2016; **6**: 21545.
- 17 Hein B, Willig KI, Hell SW. Stimulated emission depletion (STED) nanoscopy of a fluorescent protein-labeled organelle inside a living cell. *Proc Natl Acad Sci USA* 2008; **105**: 14271-14276.
- 18 Betzig E, Patterson GH, Sougrat R, Lindwasser OW, Olenych S *et al.* Imaging intracellular fluorescent proteins at nanometer resolution. *Science* 2006; **313**: 1642-1645.
- 19 Rust MJ, Bates M, Zhuang XW. Sub-diffraction-limit imaging by stochastic optical reconstruction microscopy (STORM). *Nat Methods* 2006; **3**: 793-795.
- 20 Pendry JB. Negative refraction makes a perfect lens. *Phys Rev Lett* 2000; **85**: 3966-3969.
- 21 Zhang X, Liu ZW. Superlenses to overcome the diffraction limit. *Nat Mater* 2008; **7**: 435-441.

- 22 Liu ZW, Durant S, Lee H, Pikus Y, Fang N *et al.* Far-field optical superlens. *Nano Lett* 2007; **7**: 403-408.
- 23 Rho J, Ye ZL, Xiong Y, Yin XB, Liu ZW *et al.* Spherical hyperlens for two-dimensional sub-diffractive imaging at visible frequencies. *Nat Commun* 2010; **1**: 143.
- 24 di Francia GT. Super-gain antennas and optical resolving power. *Nuovo Cim* 1952; **9**: 426-435.
- 25 Sales TRM, Morris GM. Diffractive superresolution elements. *J Opt Soc Am A* 1997; **14**: 1637-1646.
- 26 Sheppard CJR, Calvert G, Wheatland M. Focal distribution for superresolving toraldo filters. *J Opt Soc Am A* 1998; **15**: 849-856.
- 27 Zhu HF, Xu D, Wang XM, Liu WS, Yun MJ *et al.* Quasi-achromatic superresolving phase only pupil filters. *Opt Commun* 2012; **285**: 5062-5067.
- 28 Zheludev NI. What diffraction limit? *Nat Mater* 2008; **7**: 420-422.
- 29 Huang FM, Zheludev NI. Super-resolution without evanescent waves. *Nano Lett* 2009; **9**: 1249-1254.
- 30 Rogers ETF, Lindberg J, Roy T, Savo S, Chad JE *et al.* A super-oscillatory lens optical microscope for subwavelength imaging. *Nat Mater* 2012; **11**: 432-435.
- 31 Rogers ETF, Zheludev NI. Optical super-oscillations: sub-wavelength light focusing and super-resolution imaging. *J Opt* 2013; **15**: 094008.
- 32 Roy T, Rogers ETF, Zheludev NI. Sub-wavelength focusing meta-lens. *Opt Express* 2013; **21**: 7577-7582.
- 33 Yuan GH, Rogers ETF, Roy T, Adamo G, Shen ZX *et al.* Planar super-oscillatory lens for sub-diffraction circular polarization optical needles at violet wavelengths. *Sci Rep* 2014; **4**: 6333.
- 34 Huang K, Liu H, Garcia-Vidal FJ, Hong MH, Luk'yanchuk B *et al.* Ultrahigh-capacity non-periodic photon sieves operating in visible light. *Nat Commun* 2015; **6**: 7059.
- 35 Wang Q, Rogers ETF, Gholipour B, Wang CM, Yuan GH *et al.* Optically reconfigurable metasurfaces and photonic devices based on phase change materials. *Nat Photonics* 2016; **10**: 60-65.
- 36 Yuan GH, Vezzoli S, Altuzarra C, Rogers ETF, Couteau C *et al.* Quantum super-oscillation of a single photon. *Light Sci Appl* 2016; **6**: e16127.
- 37 Wong AMH, Eleftheriades GV. Advances in imaging beyond the diffraction limit. *IEEE Photonics J* 2012; **4**: 586-589.

- 38 Wong AMH, Eleftheriades GV. An optical super-microscope for far-field, real-time imaging beyond the diffraction limit. *Sci Rep* 2013; **3**: 1715.
- 39 Aharonov Y, Colombo F, Sabadini I, Struppa DC, Tollaksen J. Some mathematical properties of superoscillations. *J Phys A Math Theor* 2011; **44**: 365304.
- 40 Ferreira PJSG, Kempf A, Reis MJCS. Construction of Aharonov-Berry's super-oscillations. *J Phys A Math Theor* 2007; **40**: 5141-5147.
- 41 Berry MV, Popescu S. Evolution of quantum superoscillations and optical superresolution without evanescent waves. *J Phys A Math Gen* 2006; **39**: 6965-6977.
- 42 Berry MV, Moiseyev N. Superoscillations and supershifts in phase space: Wigner and Husimi function interpretations. *J Phys A Math Theor* 2014; **47**: 315203.
- 43 Rogers ETF, Savo S, Lindberg J, Roy T, Dennis M *et al.* Super-oscillatory optical needle. *Appl Phys Lett* 2013; **102**: 031108.
- 44 Qin F, Huang K, Wu JF, Jiao J, Luo XG *et al.* Shaping a subwavelength needle with ultra-long focal length by focusing azimuthally polarized light. *Sci Rep* 2015; **5**: 9977.
- 45 Jin NB, Rahmat-Samii Y. Advances in particle swarm optimization for antenna designs: Real-number, binary, single-objective and multiobjective implementations. *IEEE Trans Antenn Propag* 2007; **55**: 556-567.
- 46 Yuan GH, Rogers ETF, Roy T, Shen ZX, Zheludev NI. Flat super-oscillatory lens for heat-assisted magnetic recording with sub-50nm resolution. *Opt Express* 2014; **22**: 6428-6437.
- 47 Begley RF, Harvey AB, Byer RL. Coherent anti-Stokes Raman spectroscopy. *Appl Phys Lett* 1974; **25**: 387-390.
- 48 Lee DG, Ferreira PJSG. Superoscillations with optimum energy concentration. *IEEE Trans Signal Process* 2014; **62**: 4857-4867.
- 49 Bonse J, Baudach S, Krüger J, Kautek W, Lenzner M. Femtosecond laser ablation of silicon-modification thresholds and morphology. *Appl Phys A* 2002; **74**: 19-25.
- 50 Wang X, Shen ZH, Lu J, Ni XW. Laser-induced damage threshold of silicon in millisecond, nanosecond, and picosecond regimes. *J Appl Phys* 2010; **108**: 033103.
- 51 Godara P, Dubis AM, Roorda A, Duncan JL, Carroll J. Adaptive optics retinal imaging: emerging clinical applications. *Optom Vis Sci* 2010; **87**: 930-941.

Author contributions

NIZ and GHY conceived the idea of achromatic sub-diffraction focusing using super-oscillations. GHY and ETR carried out the super-oscillatory lens design and angular spectrum simulations. GHY performed the fabrication, measurements and data analysis. All authors co-wrote the paper, discussed the results and cross-edited the manuscript extensively. NIZ supervised and coordinated all the works.

Competing financial interests

The authors declare no competing financial interests.

Supplementary information accompanies the manuscript on the Light: Science & Applications website (<http://www.nature.com/lisa/>).

Figure Captions

Figure 1 Achromatic super-oscillatory lens (SOL) schemes and comparison with conventional refractive lens and diffractive optical element. (a) Dispersion of refractive lens (larger focal length for longer wavelength). (b) Opposite dispersion of diffractive optical element (larger focal length for shorter wavelength). (c) Optical SOL for achromatic focusing: two long depth-of-focus foci overlap to form the achromatic focus. (d) SOL focuses two wavelengths λ_1 and λ_2 into multiple discrete hotspots along the axial direction that spatially overlap to achieve bi-chromatic focusing.

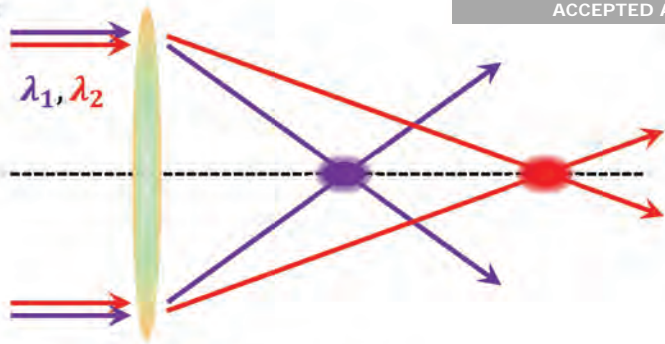
Figure 2 Near-IR achromatic fiberized amplitude-mask SOL. (a) SEM image and zoomed-in views of the SOL manufactured on the core of a single-mode large-mode-area photonic crystal fiber in which a 100 nm-thick gold film was deposited on the fiber end after cleaving. Insets in the middle figure show the fiber modes at the wavelengths of $\lambda_{IR1}=1.3 \mu\text{m}$ (top) and $\lambda_{IR2}=1.55 \mu\text{m}$ (bottom). (b) Experimental and simulated field patterns in two typical cross-sections, where the achromatic super-oscillatory hotspots are expected at $z_f=8 \mu\text{m}$. (c) Corresponding intensity profiles in the achromatic transverse focal plane.

Figure 3 Near-IR achromatic silicon phase mask SOL. (a) SEM micrograph of achromatic SOL milled on a silicon wafer, designed for achromatic focusing for wavelengths of $\lambda_{IR1}=1.3 \mu\text{m}$ and $\lambda_{IR2}=1.55 \mu\text{m}$ with working distance of $z_f=20 \mu\text{m}$. The right zoomed-in view illustrates the fabrication quality. (b) Experimental and simulated achromatic focusing behavior in the planes parallel (xz) and perpendicular (yz) to the incident polarization. (c)(d) Comparison of the hotspot size between simulations and experimental results for λ_{IR1} (c) and for λ_{IR2} (d). Insets are intensity profiles at $z_f=20 \mu\text{m}$. Blue curves are data from an angular spectrum simulation. Red and green curves show the line-scan profiles that are perpendicular and parallel, respectively, to the incident polarization (x).

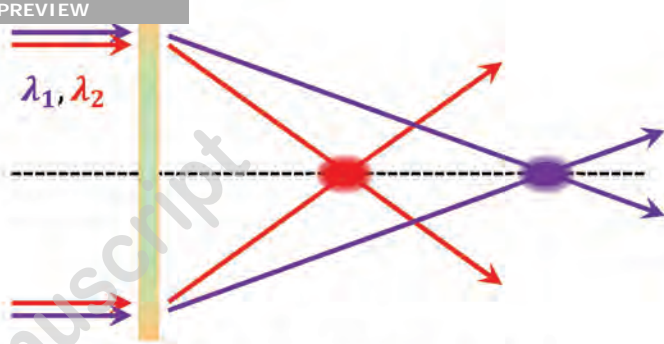
Figure 4 Visible achromatic amplitude mask SOL. (a) SEM micrograph of the fabricated mask with diameter of $80 \mu\text{m}$ and smallest ring width of 400 nm on a 100 nm -thick gold film. (b) Experimental and simulated diffraction patterns in the xz and yz cross-sections, where the achromatic super-oscillatory hotspots are generated at $z_f=18 \mu\text{m}$ for $\lambda_1=690 \text{ nm}$ and $\lambda_2=870 \text{ nm}$. (c) Corresponding field patterns in the achromatic transverse focal plane. The incident beam is x -polarized.

Figure 5 RGB ‘white’-light apochromatic amplitude mask SOL. (a) Apochromatic SOL focuses simultaneously at three different wavelengths, red ($\lambda_R=633 \text{ nm}$), green ($\lambda_G=532 \text{ nm}$) and blue ($\lambda_B=405 \text{ nm}$), that can form a ‘white’ super-oscillatory hotspot. (b) SEM micrograph of the fabricated mask with a diameter of $40 \mu\text{m}$ and a working distance of $10 \mu\text{m}$. (c)(d) Simulated (c) and experimental (d) diffraction patterns in the xz cross-section. The vertical dashed white lines indicate the focal plane. (e) Experimentally registered intensity patterns in the transverse focal plane: (e1) for λ_B , (e2) for λ_G , (e3) for λ_R , and (e4) for RGB wavelengths by simultaneously switching on the three channels. Images are captured by a color CCD camera.

a

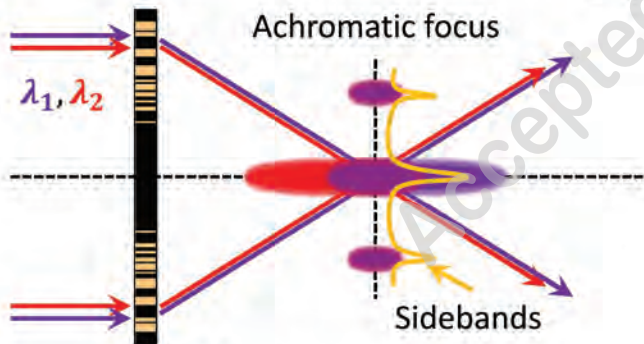


Refractive lens



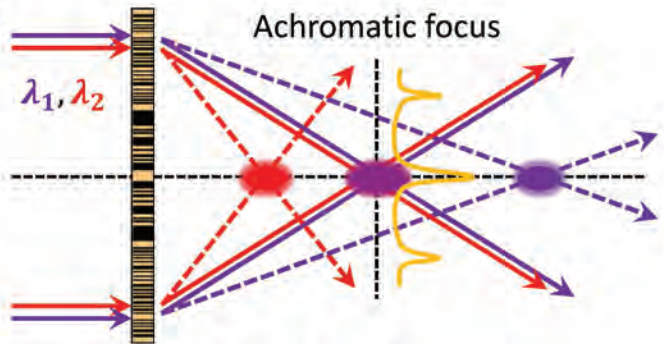
Diffractive optical element

c

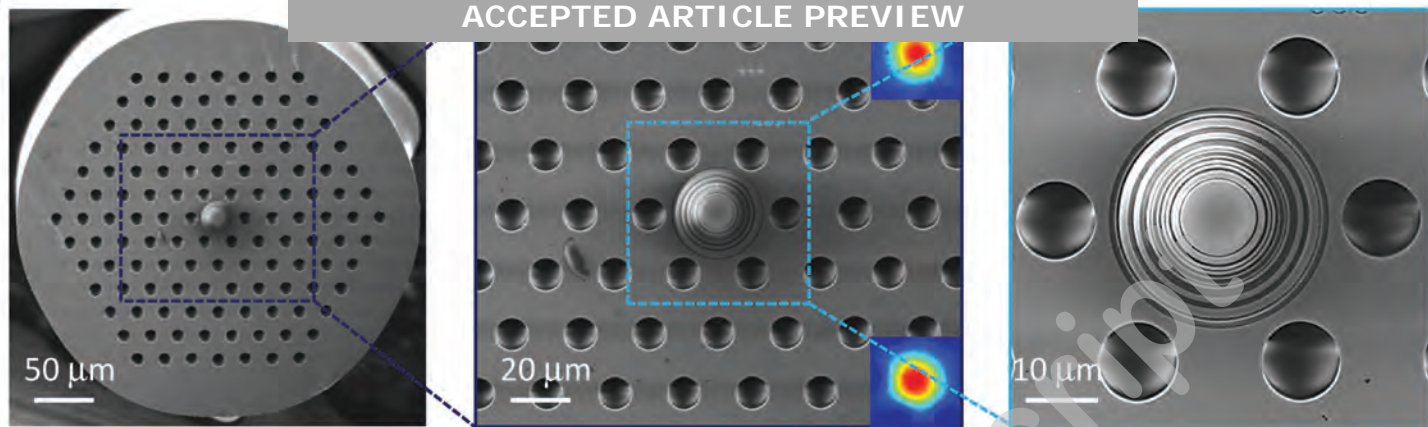
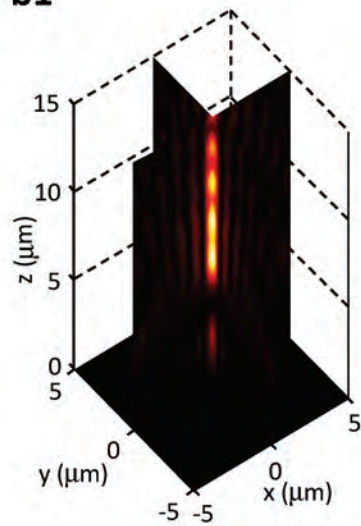
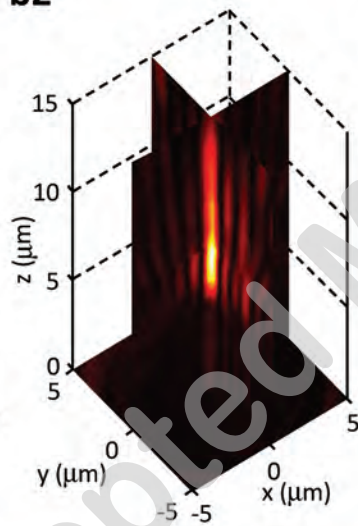
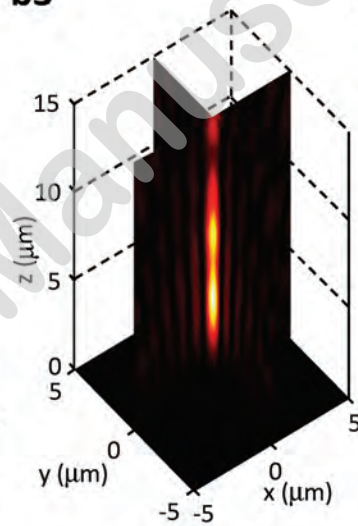
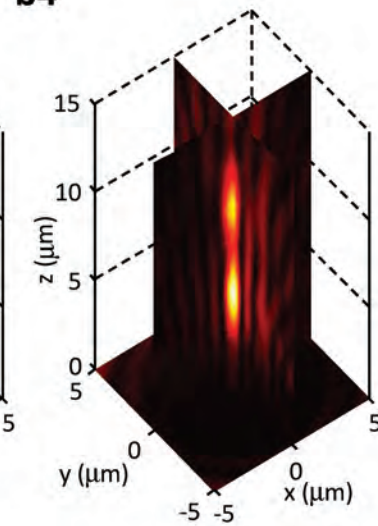


SOL: scheme 1

d



SOL: scheme 2

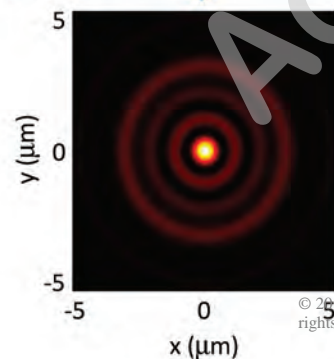
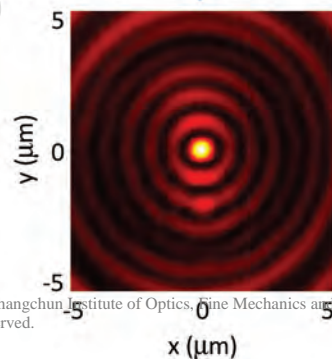
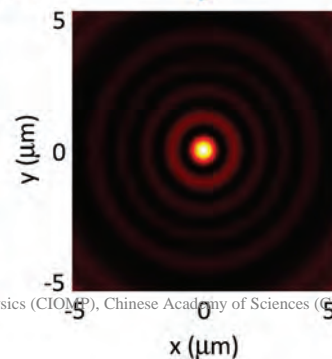
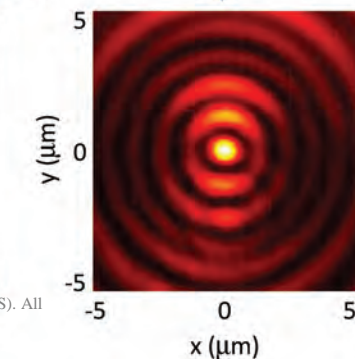
**b1****b2****b3****b4**

1300 nm (Sim.)

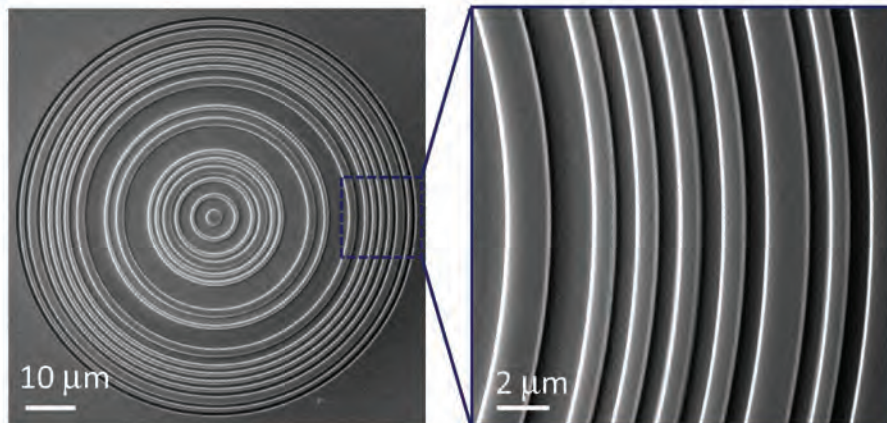
1300 nm (Exp.)

1550 nm (Sim.)

1550 nm (Exp.)

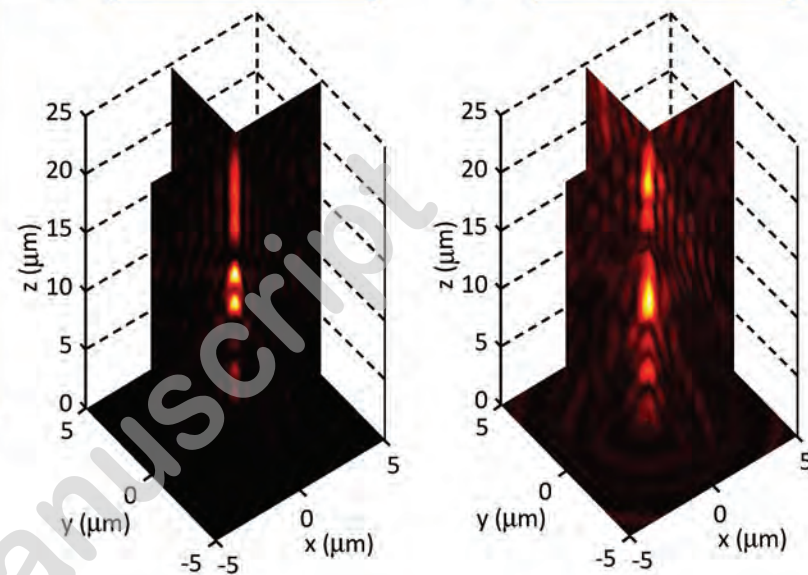
c1**c2****c3****c4**

a

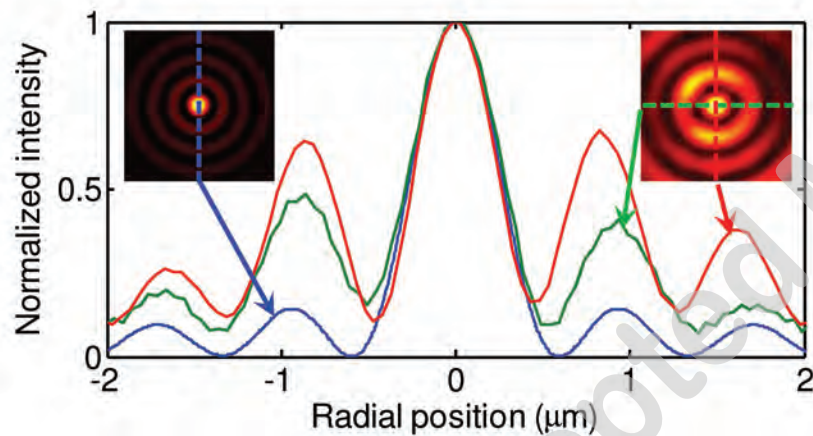


b2

1300 nm (Exp.)

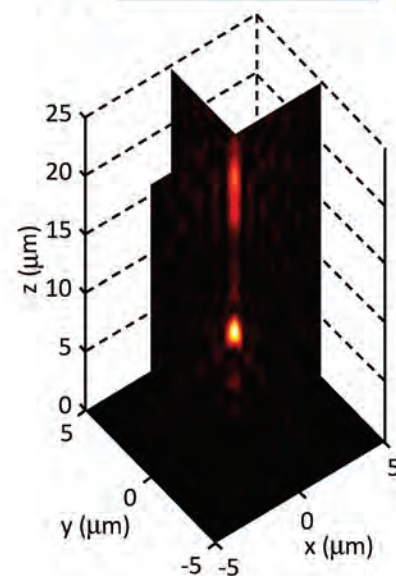


c



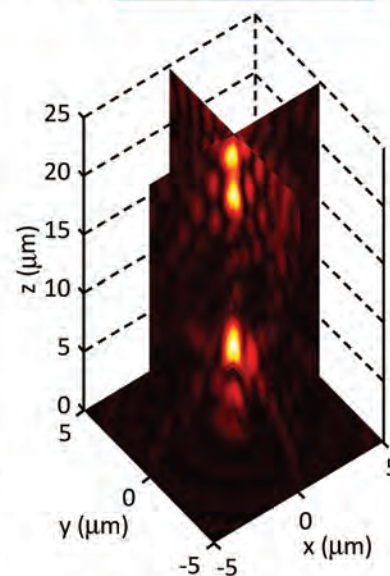
b3

1550 nm (Sim.)

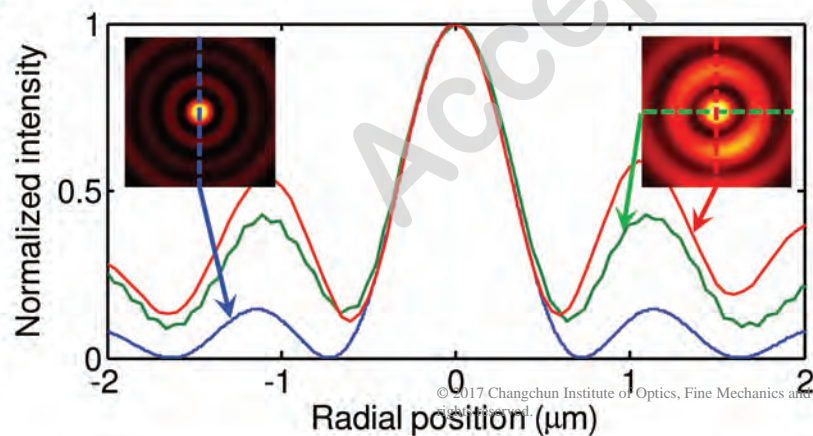


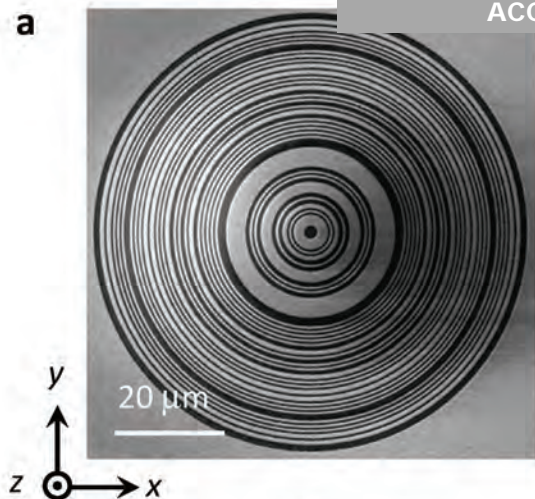
b4

1550 nm (Exp.)

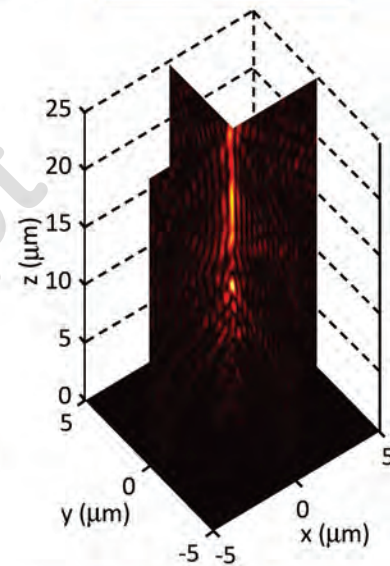
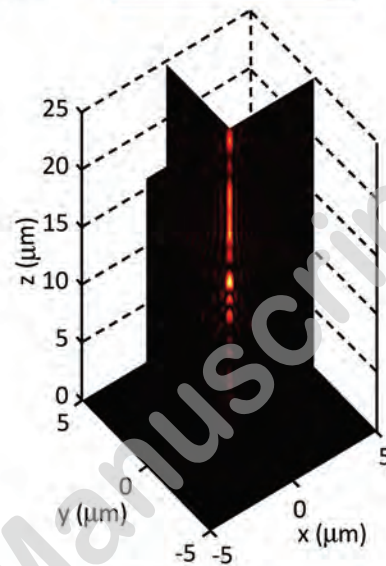


d

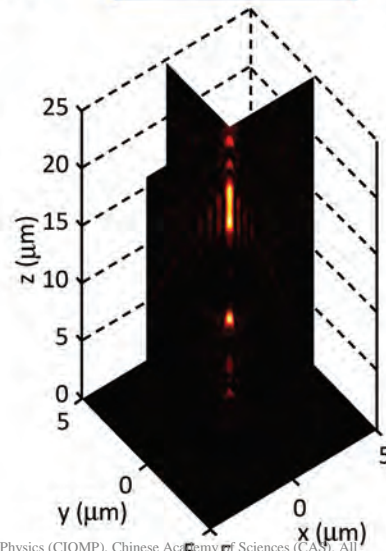


a**b2**

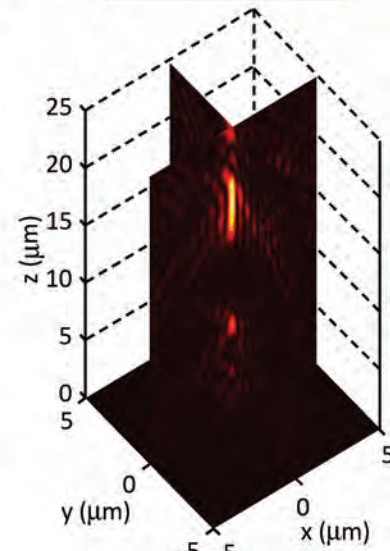
690 nm (Exp.)

**b3**

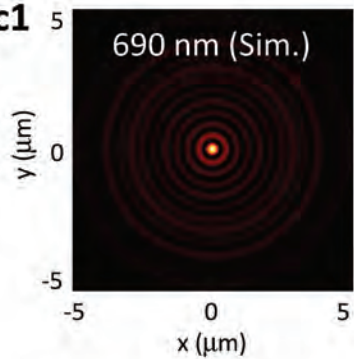
870 nm (Sim.)

**b4**

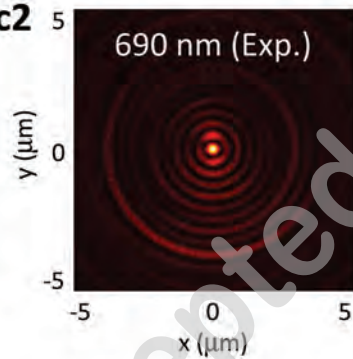
870 nm (Exp.)

**c1**

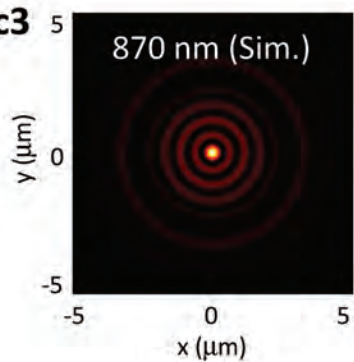
690 nm (Sim.)

**c2**

690 nm (Exp.)

**c3**

870 nm (Sim.)

**c4**

870 nm (Exp.)

